International Journal of Applied Earth Observation and Geoinformation 138 (2025) 104462

Contents lists available at ScienceDirect

International Journal of Applied Earth Observation and Geoinformation

journal homepage: www.elsevier.com/locate/jag

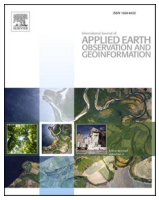

Extracting a decadal deformation on Xiaolangdi upstream dam slope using seasonally inundated distributed scatterers InSAR (SIDS – InSAR)

Lei Xie [a], Wenbin Xu [a,*], Yosuke Aoki [b]

[a] School of Geosciences and Info-physics, Central South University, China
[b] Earthquake Research Institute, The University of Tokyo, Japan

ARTICLE INFO

Keywords:
InSAR
Dam deformation
Seasonally inundated scatterer
Xiaolangdi Reservoir

ABSTRACT

Estimating deformation at the upstream dam slope from Interferometric Synthetic Aperture Radar (InSAR) is challenging due to the complete loss of coherence in seasonally inundated upstream slope. Here, we present an improved Distributed Scatterer-InSAR method that accounts for the seasonal decorrelation of upstream dam slopes and optimizes the interferogram pair selection with inter- and multi-annual baselines. We term this novel method Seasonally Inundated Distributed Scatterer InSAR (SIDS-InSAR). We apply the method with multi-sensor InSAR observations during 2007–2023 at the Xiaolangdi Reservoir (XLD), China, including Sentinel-1, ALOS-1, and ALOS-2. The results show that a new deformation map on a 1540 × 50 m^2 upstream slope in XLD, and a decaying settlement of 4.7 cm/yr (2007–2010) and 2.5 cm/yr (2015–2023), with an RMSE of 0.62 cm/yr compared to the leveling measurement. Additionally, the deformation rates are heterogeneous across the dam body as 3.7, 4.2, and 3.2 cm/yr for upstream, crest, and downstream, respectively. This study demonstrates that the SIDS-InSAR method has potential to provide a more comprehensive deformation time series of dam body, especially for the leading-edge upstream slope part.

1. Introduction

Dams bear both internal and external loads, including cyclic water loading, self-consolidation, rainfall, and aging, all of which contribute to deformation (De Sortis and Paoliani, 2007). It is crucial to monitor deformation and ensure the structural safety of dams throughout their lifespan (Tomás et al., 2013; Wang et al., 2024). Over the past seven decades, global interest in dam construction has surged due to increasing demands for power generation, flood control, and water resource management (Gao et al., 2012; Liu et al., 2023b). Currently, more than ~ 140,000 reservoirs are documented in various scientific catalogs (e.g., GranD and GOODD), and the actual number is expected to be much higher than recorded (Song et al., 2022; Wang et al., 2022). Such a massive number of dam constructions and operations pose a significant challenge for instrumental-based monitoring. Even large dams, typically considered safer, have experienced catastrophic failures worldwide, including the Oroville Dam (USA, 2017), XPXN Dam (Laos, 2020), Sardoba Dam (Uzbekistan, 2020), Derna Dam (Libya, 2023), and Nakuru Dam (Kenya, 2024) (Oduoye et al., 2024; Verma and Vijay, 2024; Xiao et al., 2022; Xie et al., 2022a, 2022b). Therefore, the development of instrument-based methods for large-scale dam deformation monitoring is urgent for hazard prevention.

Recent advancements in data processing techniques and abundance of data availability have demonstrated a wider application of Interferometric Synthetic Aperture Radar (InSAR) in routine dam monitoring and hazard early warning (Emadali et al., 2017; Milillo et al., 2016; Papoutsis et al., 2020). For example, Xie et al. (2022a) reported an accelerating deformation of 10 cm/yr two months before a dam failure event using Sentinel-1 data in the Mekong River, demonstrating the potential of InSAR as a precursory warning tool. In Sardoba dam, Uzbekistan, more localized differential subsidence of 1 cm/yr was identified from InSAR, prior to its final breach at a 200-meter section in May 2020 (Xiao et al., 2022; Xie et al., 2022b). InSAR also detected deformation in the concrete Kakhovka Dam (Ukraine), where subsidence of 8–23 mm/yr was observed starting in June 2021, and lateral movements of 5–28 mm/yr initiated in June 2022 (Tavakkoliestahbanati et al., 2024).

Although InSAR technique has proven successful in monitoring dam deformation, challenges remain due to the inadequate SAR image resolution and density of scatterers to capture the full picture of dam deformation. For the most widely used C-band SAR system such as Sentinel-1, the medium resolution of ~ 5-by-20 m can only provide,

* Corresponding author.

https://doi.org/10.1016/j.jag.2025.104462
Received 2 January 2025; Received in revised form 14 February 2025; Accepted 4 March 2025
Available online 10 March 2025

even for a mega-dam, thousands of observation pixels (Ruiz-Armenteros et al., 2021). For instance, Tavakkoliestahbanati et al. (2024) successfully identified an accelerating deformation of the Kakhovka dam in Ukraine before its collapse. However, the spatial resolution of the extracted InSAR scatterers for a concrete dam can still reach up to 100 m, potentially leading to the oversight of destabilized structures. As the vegetation, geometry distortion, soil moisture, and water inundation can directly alter properties of scattering (Shen et al., 2023), the stable permanent scatterers (PS) may degrade to distributed scatterers (DS), further decrease the available spatial coverage.

To address this, the DS-InSAR based method has been introduced to increase the spatial coverage of InSAR dam deformation (Ferretti et al., 2011; Luo et al., 2023). In the DS-InSAR workflow, spatially homogeneous pixels (SHP) are first identified by testing the similarity between neighboring pixels within a defined window. Various amplitude-based statistical methods, such as the Kolmogorov-Smirnov (KS) test, Anderson-Darling (AD) test, and Baumgartner–Wei–Schindel (BWS) test, have been employed to measure temporal variations between reference and target samples (Chen et al., 2023; Ferretti et al., 2011; Wang et al., 2012). By using confidence interval estimates of pixel's mean intensities instead of the conventional hypothesis testing for the SHP estimation further increases the speed of SHP searching (Jiang et al., 2015), although some scatterers with a similar average of amplitudes may not be subject to the same DS cluster. Therefore, several priors and assumptions have been introduced to quantify temporal features in SHP selection. For instance, Lee and Shirzaei (2023) used the standard deviation of amplitude probability density function (PDF) to classify scatterers as permanent, permanent-distributed, and distributed. Hu et al. (2019) developed a temporal detection method to adaptively select highly coherent subsets based on amplitude time series stability analysis. However, for seasonally decorrelated points due to water inundation, non-fixed periodicity or step-wise functions can be utilized to describe amplitude changes, and subset refinement methods may fail to provide a continuous network for time series analysis.

After SHP selection, phase linkage approaches, such as phase triangulation and eigenvalue decomposition, are used to optimize wrapped phase time series, with covariance matrices serving as statistical indices (Ansari et al., 2017; Ferretti et al., 2011). Thereafter, conventional network inversion methods, such as SBAS, Delaunay, and single-reference networks, are employed to estimate time-series deformation (Mirzaee et al., 2023; Reinisch et al., 2017). However, SBAS-based approaches with fixed thresholds do not always guarantee high-coherence target selection. Adaptive thresholding methods, using image- or pixel-based coherence analysis, have been proposed to minimize residual errors (Wu et al., 2019; Zhang et al., 2023). Optimization techniques, which seek to maximize overall coherence, avoid the need for threshold determination (Jiang and Guarnieri, 2020; Liang et al., 2023; Pepe et al., 2015). However, the points or interferograms with seasonal abrupt coherence loss will be considered as the decorrelated pairs, to achieve a lower cost target in the optimization (Reinisch et al., 2017; Smittarello et al., 2022; Wang et al., 2023). Consequently, even with the combination of PS-InSAR and DS-InSAR, the scatterer density can only achieve two to five times from the original SAR resolution. InSAR predominantly captures deformation on the dam crest and downstream slope (Liu et al., 2024). For instance, Liu et al. (2021) enhanced the density of scatterers on the XLD dam from ~50 m to ~30 m using the conventional DS-InSAR method. However, critical areas below the dam crest still lack reliable monitoring, with only sparse and discontinuously distributed scatterers available.

In this study, we present an improved DS-InSAR method, termed as Seasonally Inundated Distributed Scatterer InSAR (SIDS − InSAR), for extracting deformation on seasonally inundated upstream dam slope by optimizing the DS and interferogram selection. In Section 2, we describe the proposed method based on the spatial–temporal features of the seasonally inundated scatterers (SIS). Two key selection steps are presented as: 1) seasonally inundated scatterer selection, and 2) iterative minimal spanning tree (MST) pair selection. In Section 3, we introduce the study area, Xiaolangdi Reservoir, and datasets used in this study. In Section 4, we present the experimental results and evaluate performance using different methods and in-situ measurements. Section 5 discusses the deformation mechanisms and implications revealed by decadal and multi-sensor InSAR observations at XLD. We conclude the study in Section 6.

2. Method

2.1. Overview of the proposed method

To extract the deformation at seasonally inundated dam slope, we propose SIDS-InSAR method to identify the seasonally inundated scatterers from the co-registrated SLCs (Part I, Fig. 1), and an interferogram pair selection method using multiple MSTs (Part IV, Fig. 1). These two steps can be integrated into the conventional DS-InSAR workflow, such as identification of PS and DS, coherence and phase estimation, and time-series estimation.

2.2. Seasonally inundated scatterer selection

To identify seasonally inundated scatterers on the dam's upstream slope, we propose a scatterer selection method that accounts for amplitude fluctuations driven by reservoir impoundment and release cycles. According to the central limit theorem, the real and imaginary components of backscatter signals are assumed to follow Gaussian distributions with identical variance and a zero mean. Consequently, the PDF of SLC amplitudes should conform to the Rayleigh distribution (Moser et al., 2006), as follows:

$$f(A|\theta) = \frac{A}{\theta^2}\exp\left(\frac{-A^2}{2\theta^2}\right) \tag{1}$$

in which A is the amplitude, and θ is the distribution parameter that can be estimated by maximum likelihood estimation. In contrast, inundated pixels deviate from the Rayleigh distribution due to their dual scattering behavior: permanent-to-distributed-like backscattering during water recession and a complete loss of signal during inundation (Fig. 2). This results in a dual-modality amplitude pattern in the temporal domain. To capture this behavior, we employed Hartigan's Dip Statistic (HDS) method (Hartigan and Hartigan, 1985), which evaluates deviations between the empirical cumulative distribution function (eCDF) of samples and a unimodal distribution. The dip statistic is expressed as:

$$Dip(F) = \sup_x |F(x) - U(X)| \tag{2}$$

in which $F(x)$ and $U(x)$ are the eCDF of samples and closed unimodal CDF, respectively.

The corresponding p-value and the indicator function I can be expressed as follows:

$$p = \frac{1}{N}\sum_{1}^{N} I(x_i) \tag{3}$$

$$I = \begin{cases} 1, Dip(F_x) < Dip(F_U) \\ 0, Dip(F_x) \geq Dip(F_U) \end{cases} \tag{4}$$

where N is the number of samples, and the $Dip(F_x)$ and $Dip(F_U)$ are the statistics from target samples and uniform samples from bootstrap, respectively. If the p-value is greater than the significance level α, the null hypothesis H_0, indicating an unimodality distribution, will be accepted.

As the dip-test can only discriminate the unimodality for the given amplitude time series, some scatterers will be erroneously selected due to the soil moisture, vegetation, and noise. To avoid these biases, we

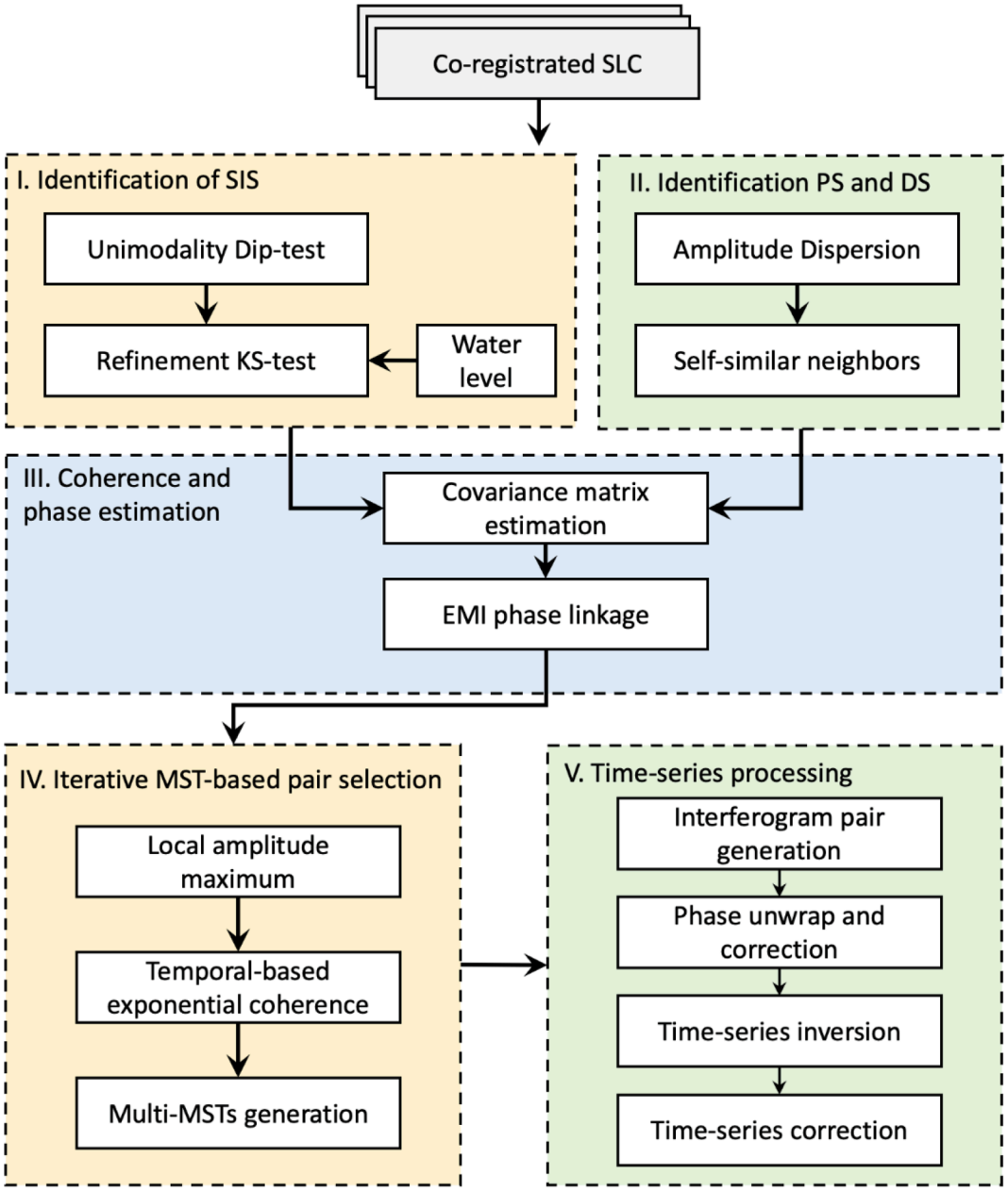

Fig. 1. Overview of the proposed SIDS-InSAR method. Two key steps are depicted in yellow boxes: 1) identification of SIS and 4) iterative MST-based interferogram selection. Note that EMI represents the Eigen decomposition-based Maximum-likelihood-estimator of Interferometric phase (Ansari et al., 2018).

further applied the nonparametric test to constrain the selected targets with a bimodality and directly reference to the water level changes in reservoir. This refinement uses the Kolmogorov–Smirnov (KS) test for the CDF of water level time series $F_w(x)$ and observed time series of amplitude $F_A(x)$, as follows:

$$D_n = max|F_A(x) - F_w(x)| \tag{5}$$

Therefore, the SIS rejected by KS distribution relative to water level time series will be removed from the non-unimodal set, ensuring that only candidates correlated with water-level changes are retained.

2.3. Iterative MST-based interferogram selection

While the short temporal baselines maintain good coherence and be sensitive to the seasonal deformation, a systematic bias may occur in the long-term deformation estimation due to error propagation. Therefore, considering the multi-annual pairs on the selected inundated points can still have a moderate-to-strong coherence (0.3–0.6), we propose a new strategy by balancing the short and long pairs of interferograms. While the coherence can be affected by multiple factors (e.g., geometry, baseline, and thermal noise), we only use the dominant temporal baselines as the factor in pair selection:

$$\begin{aligned}\gamma_{\text{total}} &= \gamma_{\text{temp}} \cdot \gamma_{\text{spatial}} \cdot \gamma_{\text{thermal}} \cdot \gamma_{\text{noise}} \\ &\simeq \gamma_{\text{temp}}\end{aligned} \tag{6}$$

Therefore, from a threshold-based perspective, the shorter temporal baselines are preferred to maintain a better coherence, which in turn discards most of the multi-annual interferograms. As the coherence behavior cannot be exactly modeled, we employ an empirical exponential model to simultaneously account decaying coherence in temporal domain (Libert, 2019), as follows:

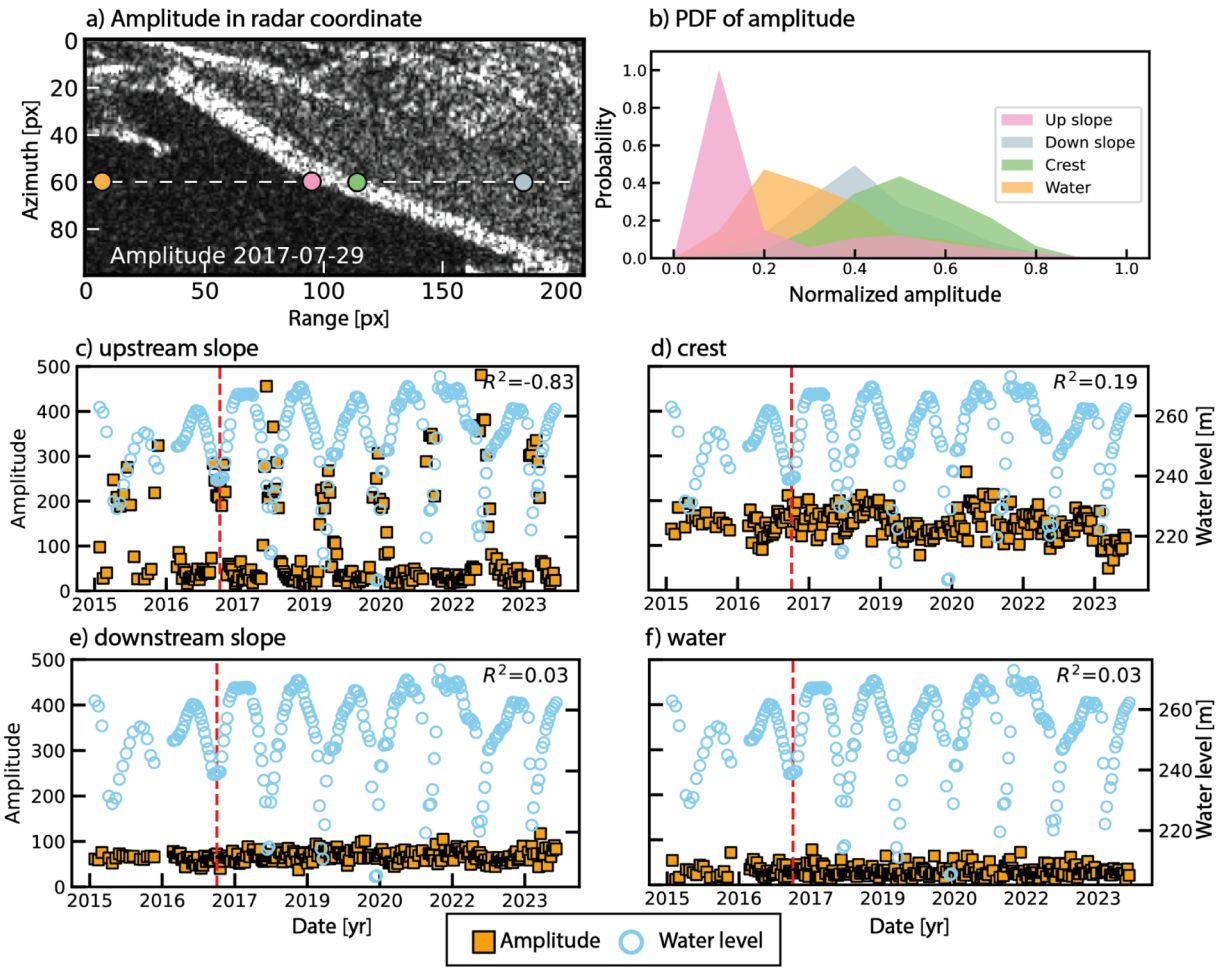

Fig. 2. An example of amplitude time series and the PDF of amplitude for the selected points: c) the upstream slope, d) the crest, e) the downstream slope, f) open water.

$$\gamma(t) = ae^{-bt} + c \tag{7}$$

in which the exponential coherence model scaled and shift the original coherence in a temporal base t days with a scaling factor a, a decaying factor b, and a shift factor c.

To exclude the acquisitions during high water standing periods, a local maximum of mean amplitudes on the selected seasonally inundated points are defined $Tmax = \{T_{m1}, T_{m2}, \cdots, T_{mk}\}$. Neighboring j acquisitions are included to enrich the residual observations of short temporal baselines. In turn, both local maximum acquisitions and their neighbors compose the selected acquisitions as:

$$T_{selected} = \{T_{m1-j}, \cdots, T_{m1}, \cdots, T_{m1+j}, \cdots, T_{mk-j}, \cdots, T_{mk}, \cdots, T_{mk+j}\} \tag{8}$$

Given the scaled proxy $1-\gamma(t)$ as the cost metric, we constructed multiple MST networks. Each SAR acquisition is treated as a node, and edges are formed by connecting $k+2j$ acquisitions, follow minimum the total cost. Up to $k+2j-1$ edges will be seleleced as a new graph representation. The first temporal interval P_0 is $[0,1)$ year to select the short pairs near the low water standing period. The next interval P_1 is $[1,2)$ years to account for the annual pairs. The remaining intervals P_i are increased with a fixed time period (e.g., 2 years) to select the pairs which is less affected by the decorrelation. Subsequently, all the pairs selected by different temporal intervals will be merged to form a complete interferogram network, as follows:

$$P_{sel} = \left\{ \bigcup_{1}^{\lceil (T_{max}-2)/t_i \rceil} P_i \right\} \bigcup P_0 \bigcup P_1 \tag{9}$$

in which T_{max} indicates the maximum temporal baselines for the selected acquisitions.

3. Study area and data process

3.1. Study area and datasets

3.1.1. The dam structure of XLD Reservoir

The Xiaolangdi Reservoir, one of the largest reservoirs in China, was selected as our study target. XLD is located at the middle reach of the Yellow River, 40 km north to the Luoyang, Henan Province, China (Fig. 3a–b). It has a maximum water storage capacity of 12.6 km^3 and a sediment storage capacity of 7.6 km^3, serving purposes such as electricity generation, irrigation, and shipping (Xu et al., 2018). The dam is an inclined clay-core dam, ranking among the world's highest rock-fill dams with a height of 160 m and a crest elevation of 283 m above sea level. The crest of dam is 1,667 m in length and 15 m in width. The foundation lies on a 70-meter overburden layer, with a concrete cutoff wall extending to a maximum depth of 82 m (Fig. 3c, Zhao, 2010). The upstream and downstream slope ratios are 1:2.6 and 1:1.75, respectively. The dam construction project began in September 1994, conducted river closure in October 1997, and the project was fully operational in December 2001 (Hu et al., 2004). The reservoir reached

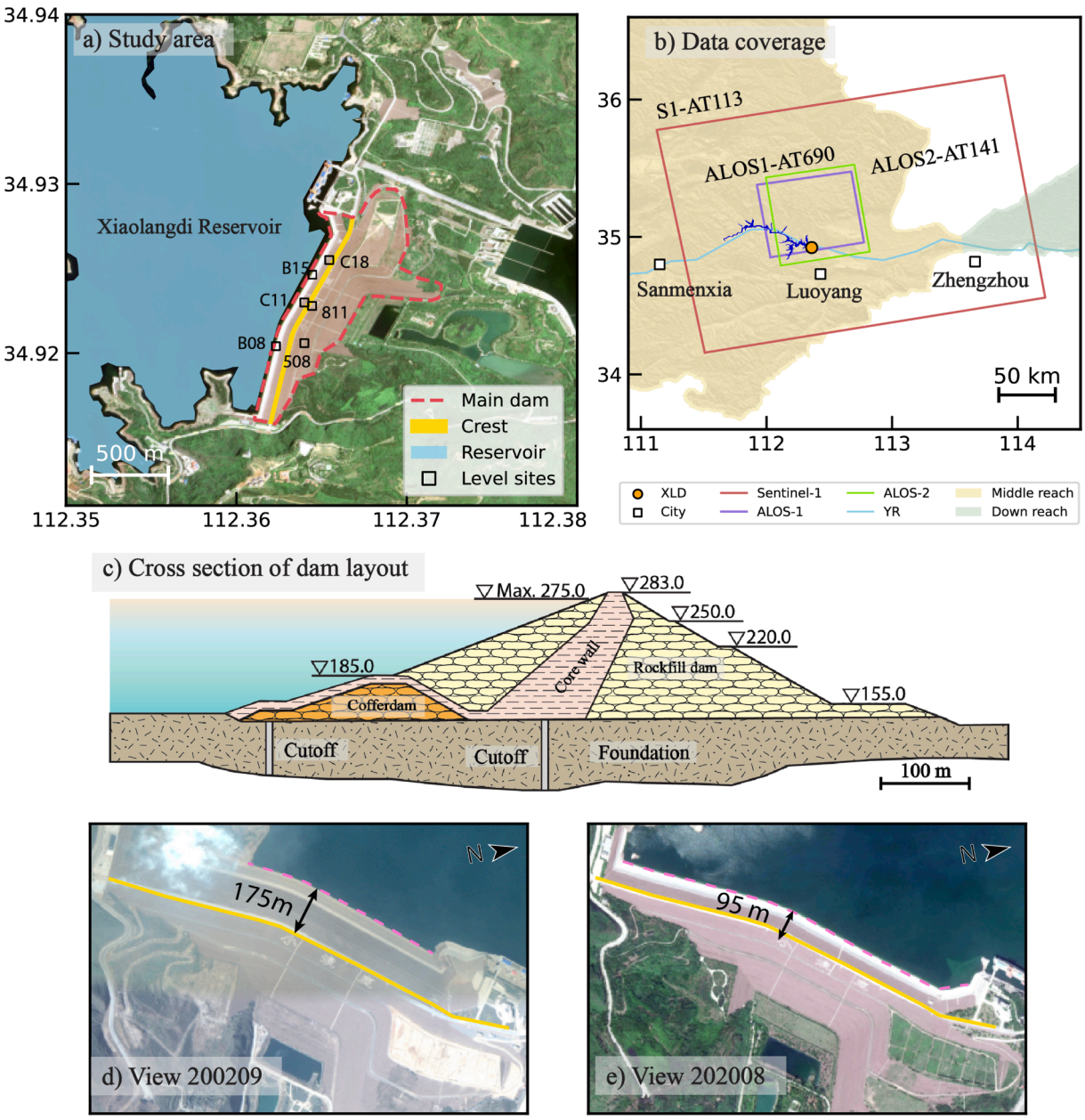

Fig. 3. Study area. a) The study area of XLD. The red dashed and yellow polygons represent the dam layout and crest, respectively. b) The footprints of SAR data. The red, purple, and green boxes denote the coverages of Sentinel-1, ALOS-1, and ALOS-2, respectively. c) Cross-section of the dam (adopted from Kong et al., 2017). d)–e) Examples of seasonal inundated upstream slopes at a low water standing in September 2002, and high water standing in August 2020. AT denotes the ascending track.

Table 1
The parameters of SAR data used in this study.

SAR	Orbit	Mode	Observation period	Scene No.	Resolution (az. by rg.)
Sentinel-1	Ascending	IW	2015/04/11–2023/12/25	225	15.6 × 2.3
ALOS-1	Ascending	Fine	2007/07/06–2010/07/14	8	9.4 × 17.7
ALOS-2	Ascending	Fine	2015/01/14–2023/10/25	15	14.4 × 17.2

its high-standing water level of 270 m in 2009.

3.1.2. SAR data

Three types of SAR sensors have been collected, including 225 scenes of Sentinel-1, 8 scenes of ALOS-1, and 15 scenes ALOS-2 during 2007 to 2023 (Table 1, and Fig. 3b). The raw SLC resolution (azimuth-by-range directions) for the Sentniel-1, ALOS-1, and ALOS-2 are 15.6 × 2.3, 9.4 × 17.7, 14.4 × 17.2 m, respectively. Due to the sparse revisit interval of ALOS series data during the low water standing period at XLD, Sentinel-1 data were prioritized for testing the performance of the proposed method. The temporal overlapped ALOS-2 data were used for cross-validation. The ALOS-1 data were used to track the deformation during 2007–2010, at which other two sensors have not been launched.

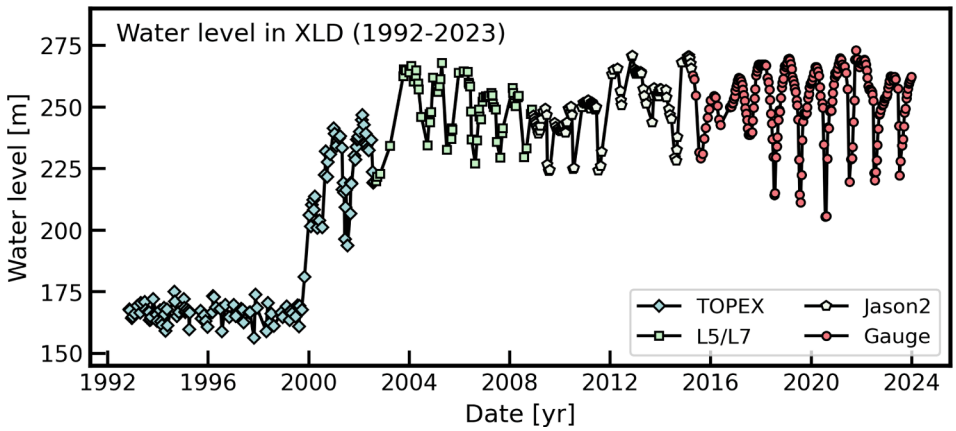

Fig. 4. Time series of water level in XLD during 1992–2023 from in-situ gauge, radar altimetry, and water-delineation.

3.1.3. Water level data

We used three types of water level data to cover the study area (Fig. 4): 1) In-situ water level data (20150411–20231225) from the bulletin of the Yellow River Water Conservancy Committee of the Ministry of Water Resources, China. 2) Radar altimetry data as TOPEX (19920930–20020808) and Jason-2 (20081214–20150324) collected from Global Reservoirs and Lakes Monitor (G-REALM). 3) Water delineation using the optical imagery of Landsat-5 and Landsat-7 (20020911–20081120) and AW3D30 DEM.

3.1.4. Leveling data

Leveling benchmark conducted between March 2017 to October 2020 were employed for examining the performance of InSAR results (He et al., 2022). There are six available leveling sites, with B08, B15 in the upstream slope at a height of 260 m; 811, C11 closed to the center of dam crest with a height of 283 m, and 508 and C18 with 200 and 400 m of distance to the central dam axis (Fig. 3a).

3.2. InSAR data processing

We utilized the InSAR Scientific Computing Environment (ISCE2) for the interferogram processing. The enhanced spectral diversity method was applied for the fine co-registration, and maintained the residual error to 1/1000 pixel (Fattahi et al., 2017). The AW3D30 DEM with 1-arc second resolution was used to remove the topographic phase component. Then, we employed the proposed method to select the SIS, and other DS candidates were identified based on local self-similarity as SHPs. The coherence matrix was estimated within local windows to avoid the bias from decorrelation noise. The phase time series recovery utilized eigenvalue decomposition and the maximum likelihood estimator as described by Ansari et al., (2018):

$$\left(\widehat{\Gamma}^{-1^{\circ}}C\right)\widehat{\zeta} = \lambda\widehat{\zeta} \tag{10}$$

in which $\widehat{\Gamma}^{-1}$ is normalization of covariance matrix, C is sample corvaraince matrix, λ is the minimum eigenvalue, and $\widehat{\zeta}$ is the corresponding eigenvector. After the phase linkage, interferograms were generated according to the network from multiple MSTs method. The optimized phase time series were unwrapped by the SNAPHU (Chen and Zebker, 2002), and corrected by a phase closure procedure with common connected component masks. We performed a weighted least square for the network inversion weighted by the covariance matrix. The tropospheric phases were decreased by the external atmospheric products GACOS (Yu et al., 2018). A second-order polynomial combined with a 1-year periodic function was used to estimate velocity.

4. Results

4.1. The result of SIS selection

The proposed method effectively identified seasonally inundated points on the upstream slope of the dam. The initial dip test detected scatterers exhibiting non-unimodal amplitude distributions. However, some candidates unrelated to the upstream slope were retained due to seasonal variations in vegetation, soil moisture, and wave-induced scattering variability (Fig. 5a). The remaining points on the water surface may come from the random errors or the waves which modify the specular reflection to the diffuse reflection. The subsequent refinement using KS test, which correlated amplitude distributions with water-level changes, excluding 38.7 % of the candidates from the dip test (Fig. 5b). Ultimately, 479 SIS points were identified on the upstream slope which covered an ~ 50 by 1240 m along the upstream dam axis (~62,000 m^2), corresponding to an average spacing of 131 m^2 per point (Fig. 5c). Although candidates close to the crest can be visually confirmed as upstream slope scatterers, they were excluded by the KS test due to weaker water-level correlations.

4.2. The result of interferogram selection

The mean amplitudes from the selected SIS were normalized to identify nine local and annual peaks (Fig. 6a), which were extended to two adjacent neighboring acquisitions (~25 days). These 36 acquisitions first formed a full stack of 630 interferograms, with coherence scaled using an exponential decay model $\gamma = 0.57 \times e^{-2.82\times10^{-4}t} + 0.041$ (Fig. 6b). The MST network selected the interferograms iteratively with increasing temporal intervals. For 0–2 years, two MSTs generated 27 and 35 pairs, respectively (Fig. 7b–c). Subsequent intervals of 2–4, 4–6, and 6–8 years produced 35, 35, and 21 pairs, respectively (Fig. 7c–f). Combining six MSTs yielded 153 interferograms (Fig. 7g), creating a balanced network that incorporated both short and long temporal baselines.

4.3. Comparison and validation

First, we compared the estimated velocities from the proposed method with the Delaunay and SBAS networks (i.e., with a maximum temporal baseline of 430 days, and spatial baseline of 200 m). There are 99 and 183 pairs of interferograms generated from the Delaunay and SBAS networks (Fig. 8b–c). The velocities were estimated by the same second-order polynomial with a 1-year periodic function. From the proposed iterative MSTs network, we effectively captured significant deformation on the upstream slope (350 × 60 m), with maximum LOS velocities ranging from 1.5–2 cm/yr (Fig. 8d). In comparison, the

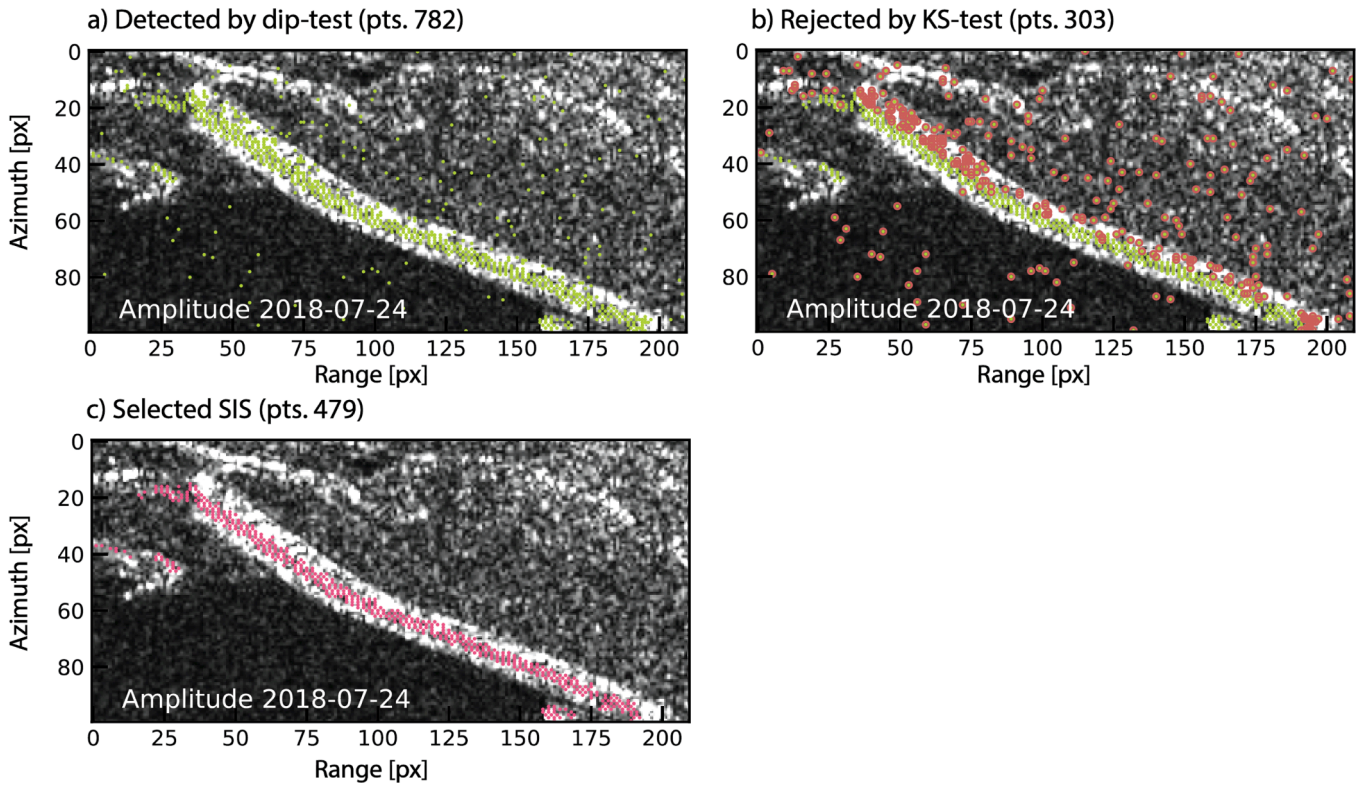

Fig. 5. The selected seasonally inundated scatterers on the upstream slopes: a) The candidates using unimodality dip-test; b) The candidates rejected by the KS-test (brown points); c) the final selection of SIS.

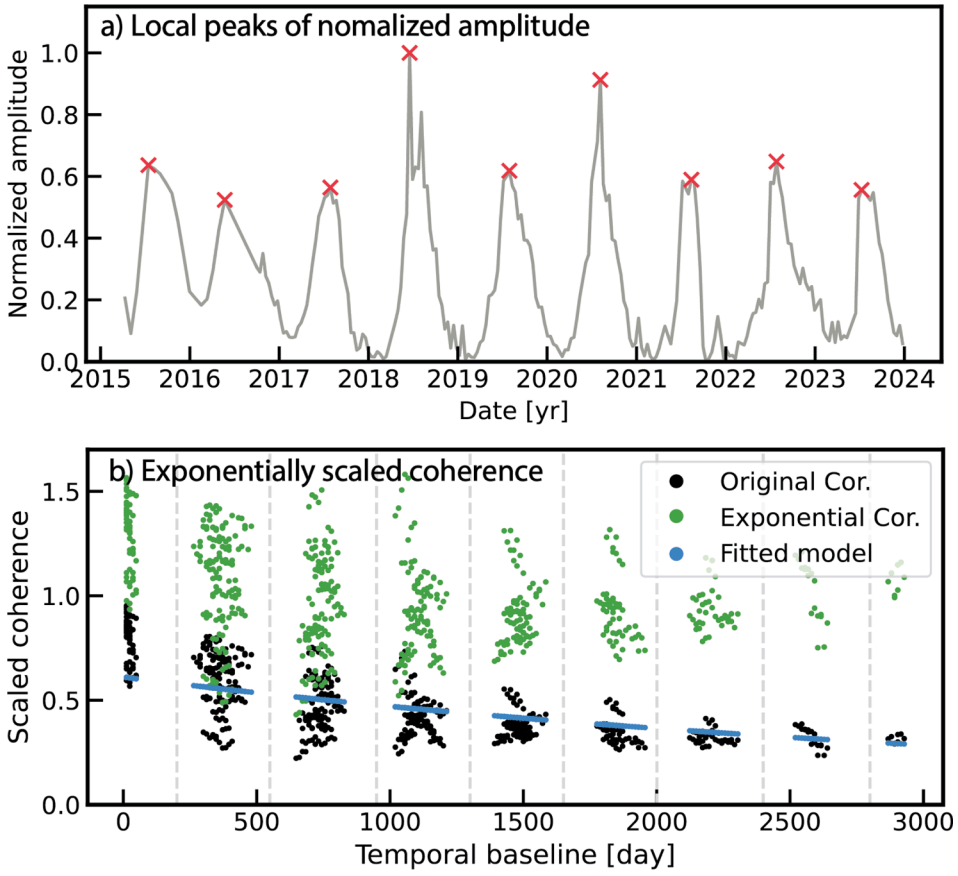

Fig. 6. Annual amplitude peaks and coherence with exponential model for interferogram pair connections.

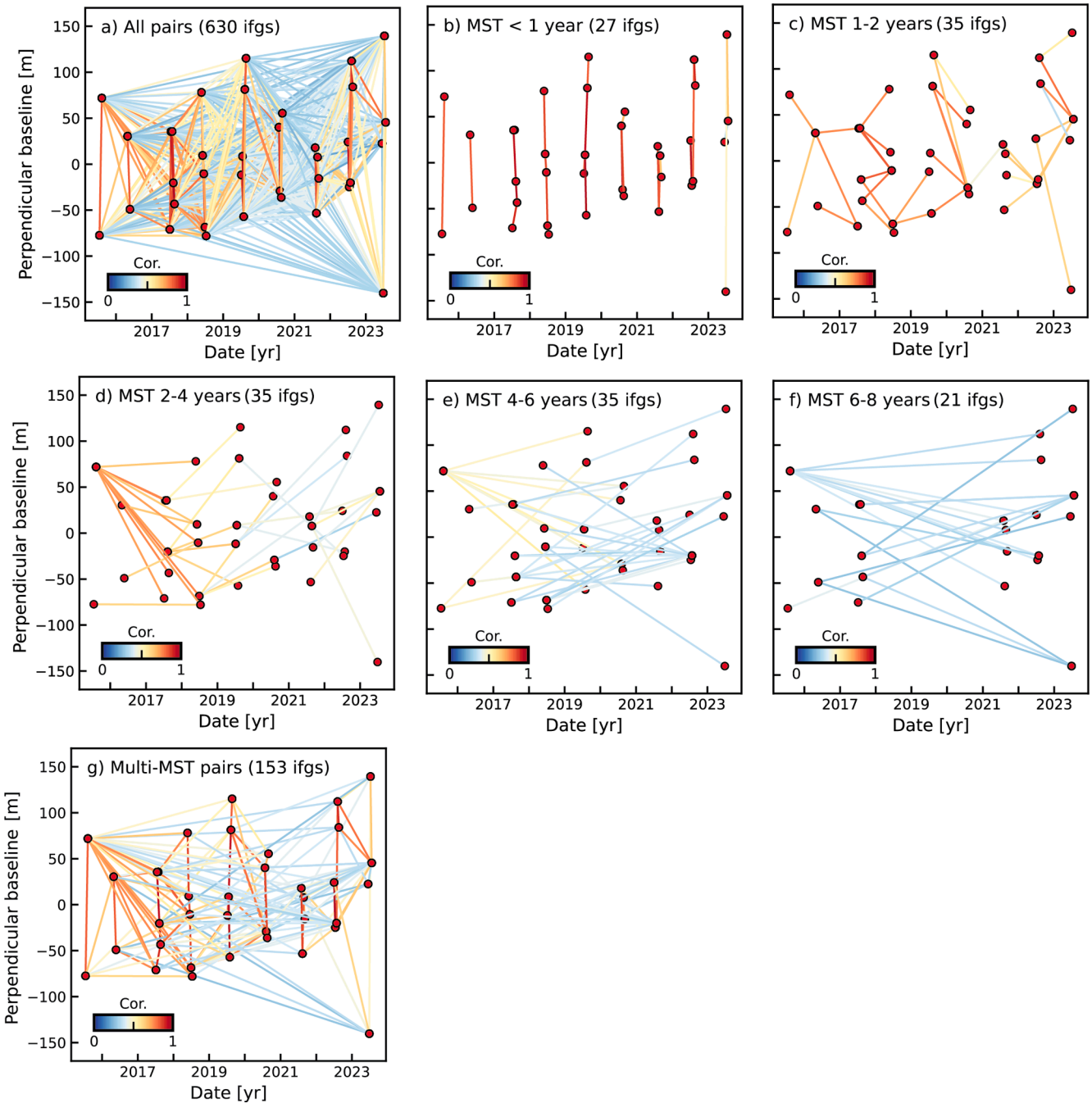

Fig. 7. Interferogram pair selection. a) Full connection of interferogram pairs; b) –f) the step-by-step selection; g) the proposed method.

Delaunay network underestimated deformation with maximum rates of 0.77 cm/yr at the middle section of the dam axis, and 85.2 % of points exhibiting a velocity difference below 0.5 cm/yr (Fig. 8e and 8g). The SBAS network showed a more consistent deformation pattern with the proposed method that 88.1 % of velocity discrepancy was less than 0.5 cm /yr (Fig. 8f and 8 h).

Similar to the upstream slope, the deformation estimated from the proposed method in the crest and the downstream slope has a more significant deformation and concentrated pattern, with maximum LOS deformation of ~ 3.1 cm/yr (Fig. 9a). Validation against leveling measurements conducted between March 2017 and October 2020 revealed that the proposed method achieved the lowest RMSE (0.62 cm/yr), outperforming the SBAS (0.92 cm/yr) and Delaunay (1.24 cm/yr) networks (Fig. 9e). Notably, at locations near crest with intensive deformation (e.g., C11 and 811), the proposed method exhibited minimal deviation of 1.15 cm/yr and 0.43 cm/yr (Fig. 9d-e). The observed underestimation of InSAR-derived measurements compared to in-situ data was primarily attributed to coarse spatial resolution averaging, which may introduce the lower estimates and systematic bias in highly deformed area (Zheng et al., 2022).

4.4. *Temporal variation of dam deformation*

To better illustrate the deformation evolutions of the dam, we followed the conventional SBAS method to process the ALOS-1 and ALOS-2 data for the reason that a sparse temporal coverage does not allow for a DS-like processing. The ALOS-1 data (2007–2010) showed vertical deformation rates from − 4.7 cm/yr to − 2.7 cm/yr near the main axis of

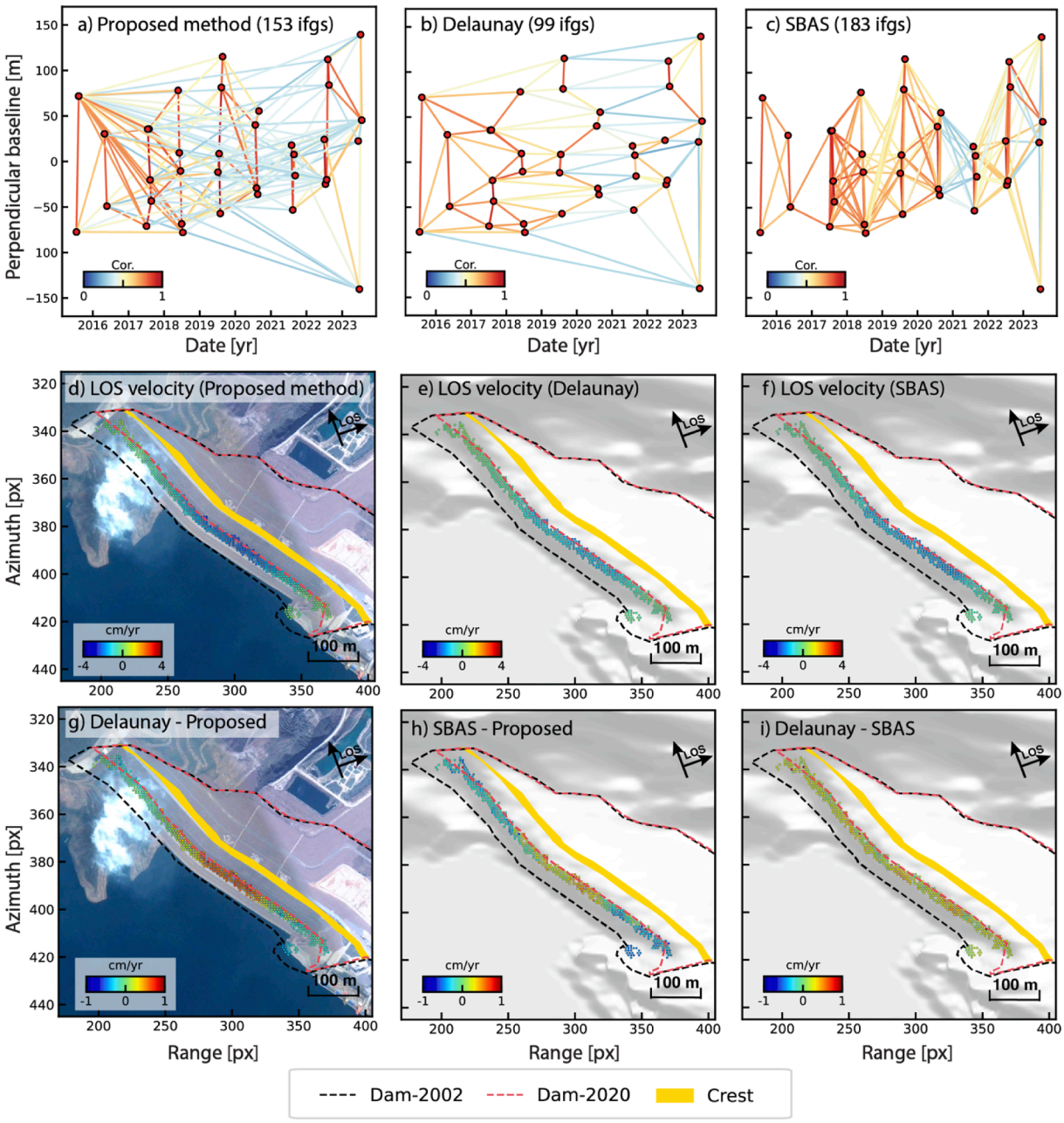

Fig. 8. The comparisons of estimated deformation velocity on the upstream slope using different network configurations. Row 1: the baseline configuration. Row 2: the estimated LOS velocity. Row 3: the difference of estimated velocity maps. The dashed black and red lines denote the seasonal exposed dam structures in 2002 and 2020, respectively.

the dam body (Fig. 10a). Between 2015 and 2023, both Sentinel-1 and ALOS-2 indicated similar decelerated trends with vertical deformation rates ranging from − 3.2 cm/yr to − 2 cm/yr (Fig. 10b–c). Specifically, the upstream slopes at elevations of 250–283 m, showed a distinct deceleration from − 3.7 cm/yr to − 2.7 cm/yr between periods of 2007–2010 and 2015–2023. The dam crest experienced a more pronounced decelerated deformation from − 4.7 cm/yr to − 2.5 cm/yr. The downstream slope at elevation, from 250 to 283 m, demonstrated similar decelerating trends from 3.2 cm/yr to 1.7 cm/yr.

Temporally, we employed the full stack of Sentinel-1 data (225 scenes) with temporal resolution of 12–24 days to replace the selected 36 scenes during low water-standing periods. It enables a more fined seasonal deformation estimation due to water level changes in the crest and downstream slopes (Fig. 11, grey dots). All validated leveling points exhibited a strong negative correlation (ranging from 0.5 to 0.8), indicating that deformation in the vertical direction was modulated by static stress from water loading. The amplitude of seasonal deformation was found to be proportional to the amplitude of water level fluctuations. For instance, during 2017–2018, when water levels ranged from 238 to 267 m, the seasonal displacement was approximately ± 12 mm. In 2018–2019, as water levels fluctuated more significantly (214–267 m), seasonal deformation increased to approximately ± 18 mm.

5. Discussion

In this section, we discussed the driving factors for the long-term and seasonal deformation of the XLD dam as revealed by multi-sensor InSAR observations. The long-term deformation by the ALOS series and Sentinel-1 data reveals a decelerating subsidence across all major sections of the dam body from Period I (2007–2010) to Period II

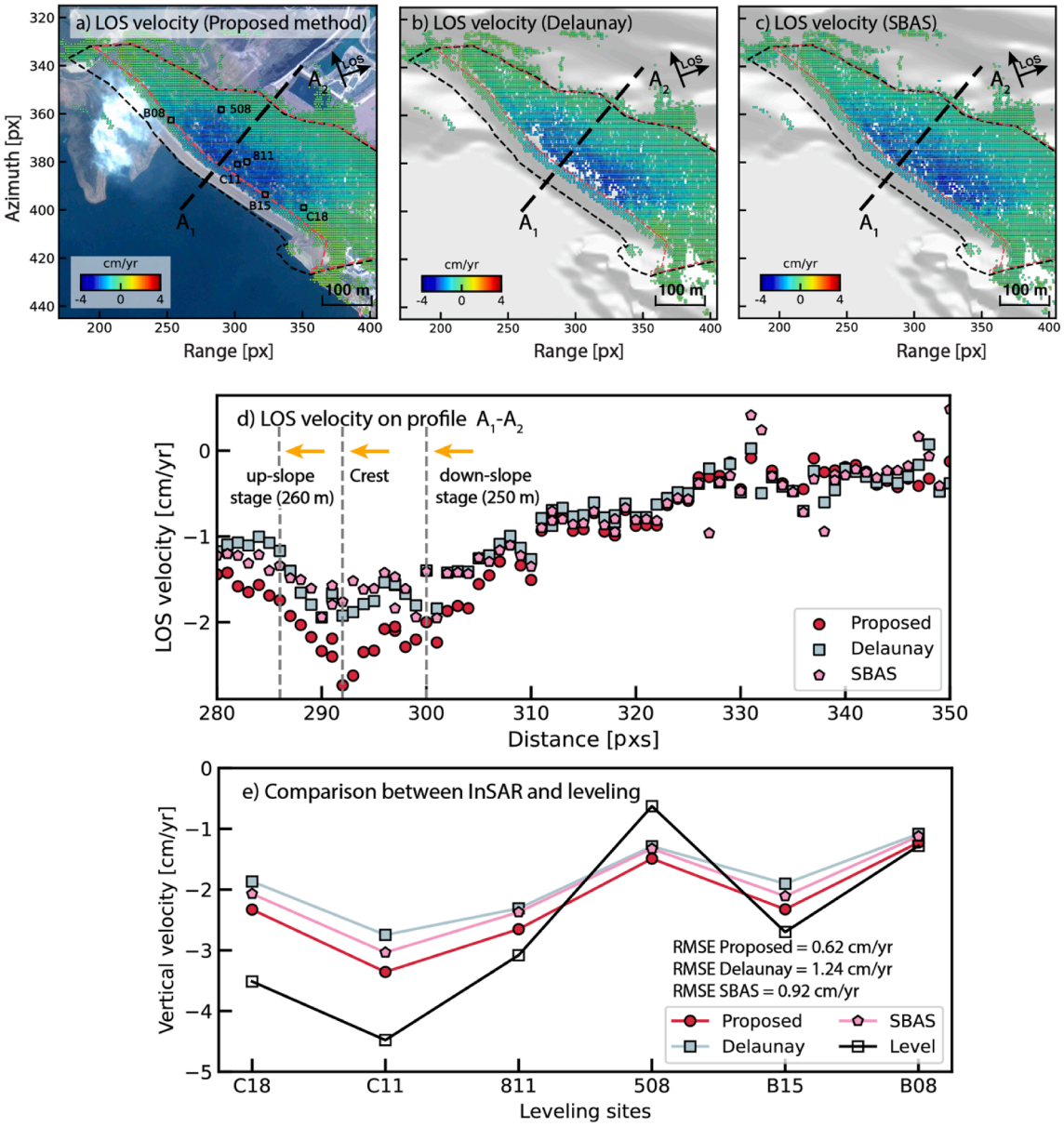

Fig. 9. The validation of estimated deformation velocity across the dam: a–c) the estimated LOS deformation; d) the displacement along profile A_1–A_2; e) the validation with leveling data. The unit of distance is pixel in radar coordinate.

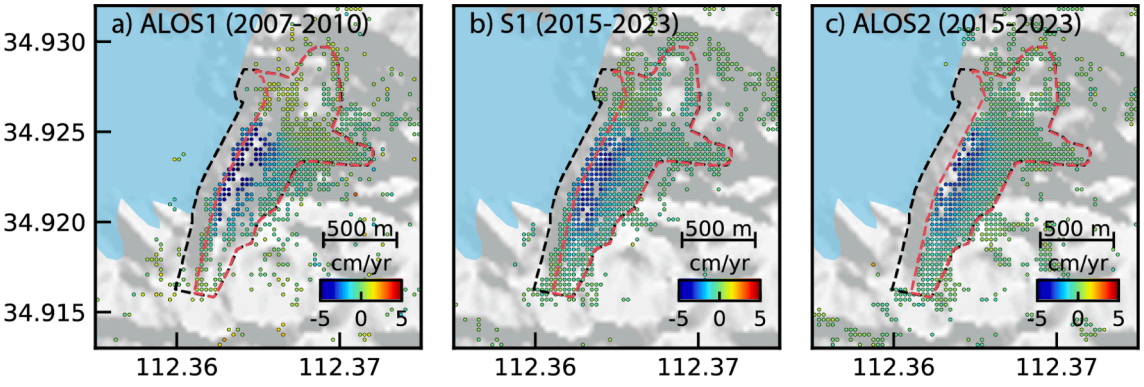

Fig. 10. The decaying vertical deformation from different sensors during 2007–2023: a) ALOS1 (2007–2010); b) Sentinel-1 (2015–2023); c) ALOS-2 (2015–2023).

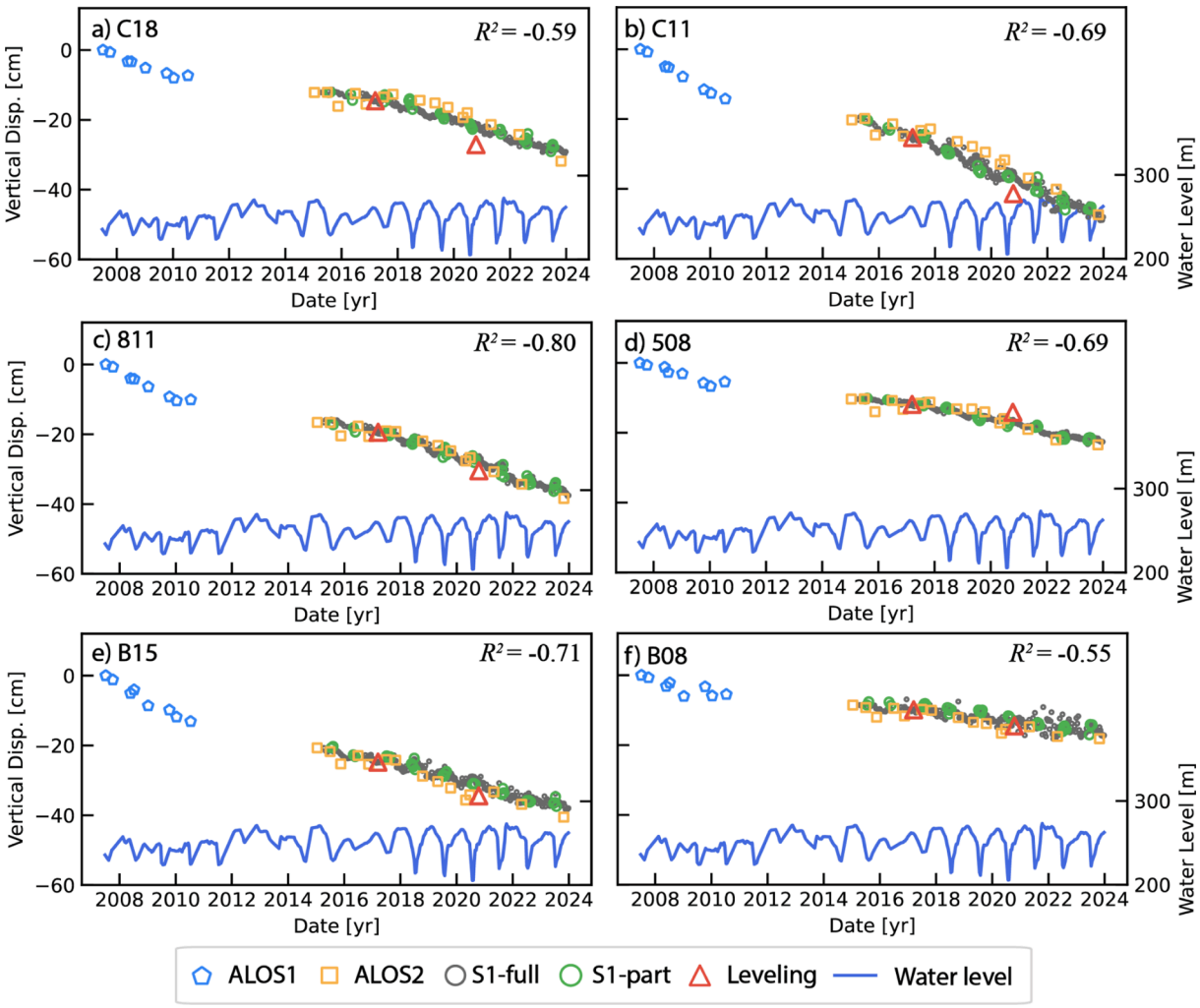

Fig. 11. The time series vertical deformation from different sensors and the leveling measurements. Noted that the S1-full represent the full stack of 225 images, and the S1-part denotes the selected 36 scenes acquired at the low water standing period.

(2015–2023). For instance, C11 at the upstream slope, InSAR results indicate a subsidence of 4.8 cm/yr in Period I to 3.3 cm/yr in Period II. Compared to previous InSAR investigations at the XLD dam, Liu et al. (2021) and Luo et al. (2023) reported a similar subsidence rate of 2–3 cm/yr at the crest of XLD dam. However, the decadal decaying subsidence cannot be adequately captured by Sentinel-1 data alone. Although there is a 1.1 cm/yr underestimation compared to leveling data from 2018 to 2019, the temporal decaying trend is evident. Considering leveling data after the initial impoundment from 2004 to 2006 (Zhao, 2010), the same leveling line at 283 m on the upstream side shows a subsidence of 8.5 cm/yr, also indicating a clear exponential decay. Therefore, this long-term settlement documented by InSAR in recent decade is supposed related to the compression of soil layers under sustained self-gravity loading (Hu et al., 2017; Terzaghi et al., 1996).

Despite the temporal deceleration, the observed vertical deformation rates in key structures are 3.7 cm/yr for the upstream slope, 4.7 cm/yr for the crest, and 3.2 cm/yr for the downstream slope. This also suggests the observed deformation is influenced by the filling height of the dam body (Liu et al., 2023a). Comparison of C11 and 811 sites on the same elevation of 283 a.s.l but for upstream and downstream slopes, the 1 cm/yr larger subsidence is likely caused by water pressure directly acting on the slope or deformation from shallow sediments (Lin et al., 2023), rather than self-weight-induced consolidation (Tedd et al., 1997).The findings indicate that deformation in the XLD dam over the past decade is governed by both long-term and seasonal factors: 1) Consolidation related to the filling height and material properties of the dam body; 2) Water loading, which exerts static pressure on the upstream slope and induces bending of the foundation; 3) Shallow sediment compaction predominantly affecting the upstream slope. It also highlights advantages of the proposed method in providing a more comprehensive view of dam structure by a dense scatterer coverage, particularly in the upstream slope with ~ 100 m^2 per point. As a result, the observed heterogeneous deformation can reflect the structural complexity of the dam and the spatial distribution of the water body.

6. Conclusion

In this study, we present an enhanced InSAR time series approach, termed SIDS-InSAR, for extracting deformation of seasonally inundated dam slopes. The method incorporates two key advancements in the conventional DS-InSAR processing workflow: (1) identification of seasonally inundated scatterers through a two-step statistical testing process, which enables the effective InSAR monitoring in dam's upstream slope; and (2) integration of multiple MSTs to optimize velocity estimation by balancing short and long temporal baselines, thereby improving the deformation monitoring accuracy through optimized baseline configuration. We applied the proposed method to the Xiaolangdi Reservoir using Sentinel-1 data from 2015 to 2023. The approach effectively captured deformation in the upstream slope, achieving a density of 131 m^2 per point over the upstream slope area of 62,000 m^2.

The extracted heterogeneous deformation across different structures of dam body rates of −5 to −2 cm/yr were validated against leveling data and other methods, demonstrating improved accuracy with residuals of 0.62 cm/yr. Additionally, we combined the ALOS-1/2 data to capture the decadal deformation evolution since 2007, revealing a decaying settlement of 4.7 cm/yr to 2.5 cm/yr from 2007 to 2023. In summary, the proposed SIDS-InSAR method and decadal InSAR observations enable the characterization of heterogeneous dam deformation patterns in both temporal and spatial domains. This approach facilitates the identification of deformation drivers, such as seasonal water loading, dam structure, and consolidation, thereby contributing to the improved management and safety assessment of hydraulic infrastructure.

CRediT authorship contribution statement

Lei Xie: Writing – review & editing, Writing – original draft, Software, Methodology, Investigation, Formal analysis, Conceptualization. **Wenbin Xu:** Writing – review & editing, Investigation, Formal analysis. **Yosuke Aoki:** Writing – review & editing, Investigation, Formal analysis, Data curation.

Declaration of competing interest

The authors declare that they have no known competing financial interests or personal relationships that could have appeared to influence the work reported in this paper.

Acknowledgements

The research is supported by the National Natural Science Foundation of China (42304037, 42174023), National Key Research and Development Program (2022YFB3903602), Frontier Cross Research Project of Central South University (2023QYJC006), Hunan Province Dam Safety and Disease Prevention Engineering Research Center (Hndam2023kf05), and Natural Science Foundation of Hunan Province (2024JJ3031, 2025JJ60239). We thank for the ESA, JAXA, and USGS for the Sentinel-1, ALOS-1/2, and Landsat-5/7 data. The radar altimetry data are from Global Reservoirs and Lakes Monitor (G-REALM) (doi: ipad.fas.usda.gov/cropexplorer/global_reservoir/gr_regional_chart.aspx?regionid=che&reservoir_name=Xiaolangdi&lakeid=002282), the gauge measurements are from the Yellow River Water Conservancy Committee of the Ministry of Water Resources, China (http://61.163.88.227:8006/hwsq2.aspx?sr=0nkRxv6s9CTRMlwRgmfFF6jTpJPtAv87).

Data availability

Data will be made available on request.

References

Ansari, H., De Zan, F., Bamler, R., 2018. Efficient phase estimation for interferogram stacks. IEEE Trans. Geosci. Remote Sens. 56, 4109–4125. https://doi.org/10.1109/TGRS.2018.2826045.

Ansari, H., De Zan, F., Bamler, R., 2017. Sequential estimator: toward efficient InSAR time series analysis. IEEE Trans. Geosci. Remote Sens. 55, 5637–5652. https://doi.org/10.1109/TGRS.2017.2711037.

Chen, B., Yang, J., Li, Z., Yu, C., Yu, Y., Qin, L., Yang, Y., Yu, H., 2023. A new sequential homogeneous pixel selection algorithm for distributed scatterer InSAR. Giscience Remote Sens. 60, 2218261. https://doi.org/10.1080/15481603.2023.2218261.

Chen, C.W., Zebker, H.A., 2002. Phase unwrapping for large SAR interferograms: statistical segmentation and generalized network models. IEEE Trans. Geosci. Remote Sens. 40, 1709–1719. https://doi.org/10.1109/TGRS.2002.802453.

De Sortis, A., Paoliani, P., 2007. Statistical analysis and structural identification in concrete dam monitoring. Eng. Struct. 29, 110–120. https://doi.org/10.1016/j.engstruct.2006.04.022.

Emadali, L., Motagh, M., Haghshenas Haghighi, M., 2017. Characterizing post-construction settlement of the Masjed-Soleyman embankment dam, Southwest Iran, using TerraSAR-X SpotLight radar imagery. Eng. Struct. 143, 261–273. https://doi.org/10.1016/j.engstruct.2017.04.009.

Fattahi, H., Agram, P., Simons, M., 2017. A network-based enhanced spectral diversity approach for TOPS time-series analysis. IEEE Trans. Geosci. Remote Sens. 55, 777–786. https://doi.org/10.1109/TGRS.2016.2614925.

Ferretti, A., Fumagalli, A., Novali, F., Prati, C., Rocca, F., Rucci, A., 2011. A new algorithm for processing interferometric data-stacks: SqueeSAR. IEEE Trans. Geosci. Remote Sens. 49, 3460–3470. https://doi.org/10.1109/TGRS.2011.2124465.

Gao, H., Birkett, C., Lettenmaier, D.P., 2012. Global monitoring of large reservoir storage from satellite remote sensing. Water Resour. Res. 48, 2012WR012063. https://doi.org/10.1029/2012WR012063.

Hartigan, J.A., Hartigan, P.M., 1985. The dip test of unimodality. Ann. Stat. 13, 70–84. https://doi.org/10.1214/aos/1176346577.

Hu, F., Wu, J., Chang, L., Hanssen, R.F., 2019. Incorporating temporary coherent scatterers in multi-temporal InSAR using adaptive temporal subsets. IEEE Trans. Geosci. Remote Sens. 57, 7658–7670. https://doi.org/10.1109/TGRS.2019.2915658.

Hu, X., Oommen, T., Lu, Z., Wang, T., Kim, J.-W., 2017. Consolidation settlement of Salt Lake County tailings impoundment revealed by time-series InSAR observations from multiple radar satellites. Remote Sens. Environ. 202, 199–209. https://doi.org/10.1016/j.rse.2017.05.023.

Jiang, M., Ding, X., Hanssen, R.F., Malhotra, R., Chang, L., 2015. Fast statistically homogeneous pixel selection for covariance matrix estimation for multitemporal InSAR. IEEE Trans. Geosci. Remote Sens. 53, 1213–1224. https://doi.org/10.1109/TGRS.2014.2336237.

Jiang, M., Guarnieri, A.M., 2020. Distributed scatterer interferometry with the refinement of spatiotemporal coherence. IEEE Trans. Geosci. Remote Sens. 58, 3977–3987. https://doi.org/10.1109/TGRS.2019.2960007.

Kong, D., Miao, C., Wu, J., Borthwick, A.G.L., Duan, Q., Zhang, X., 2017. Environmental impact assessments of the Xiaolangdi reservoir on the most hyperconcentrated laden river, Yellow River, China. Environ. Sci. Pollut. Res. 24, 4337–4351. https://doi.org/10.1007/s11356-016-7975-4.

Lee, J.-C., Shirzaei, M., 2023. Novel algorithms for pair and pixel selection and atmospheric error correction in multitemporal InSAR. Remote Sens. Environ. 286, 113447. https://doi.org/10.1016/j.rse.2022.113447.

Liang, H., Zhang, L., Li, X., 2023. Enhancing MTInSAR phase unwrapping in decorrelating environments by spatiotemporal observation optimization. IEEE Geosci. Remote Sens. Lett. 20, 1–5. https://doi.org/10.1109/LGRS.2023.3244824.

Lin, S.-Y., Chang, S.-T., Lee, C.-F., 2023. InSAR-based investigation on spatiotemporal characteristics of river sediment behavior. J. Hydrol. 617, 129076. https://doi.org/10.1016/j.jhydrol.2023.129076.

Libert, L., 2019. Towards Operational Use of Combined Split-Band Interferometry and Multidimensional Small Baseline Subset (Doctoral thesis). University of Liège.

Liu, Y., Fan, H., Wang, L., Zhuang, H., 2021. Monitoring of surface deformation in a low coherence area using distributed scatterers InSAR: case study in the Xiaolangdi Basin of the Yellow River, China. Bull. Eng. Geol. Environ. 80, 25–39. https://doi.org/10.1007/s10064-020-01929-1.

Liu, H., Zhu, M., Zhu, W., Zhao, W., Bai, Z., Zhou, B., Li, G., Wang, Y., 2023a. Soil and Rockfill dams safety assessment for Henan province: monitoring, analysis and prediction. Remote Sens. 15, 4293. https://doi.org/10.3390/rs15174293.

Liu, X., Li, Z., Sun, L., Khailah, E.Y., Wang, J., Lu, W., 2023b. A critical review of statistical model of dam monitoring data. J. Build. Eng. 80, 108106. https://doi.org/10.1016/j.jobe.2023.108106.

Liu, J., Li, T., Ma, S., Shan, Q., Jiang, W., 2024. Study on LOS to vertical deformation conversion model on embankment slopes using multi-satellite SAR interferometry. ISPRS Int. J. Geo Inf. 13, 58. https://doi.org/10.3390/ijgi13020058.

Luo, J., Lopez-Sanchez, J.M., De Zan, F., 2023. Analysis of the performance of polarimetric PSI over distributed scatterers with Sentinel-1 data. Int. J. Appl. Earth Obs. Geoinformation 125, 103581. https://doi.org/10.1016/j.jag.2023.103581.

Milillo, P., Perissin, D., Salzer, J.T., Lundgren, P., Lacava, G., Milillo, G., Serio, C., 2016. Monitoring dam structural health from space: Insights from novel InSAR techniques and multi-parametric modeling applied to the Pertusillo dam Basilicata, Italy. Int. J. Appl. Earth Obs. Geoinformation 52, 221–229. https://doi.org/10.1016/j.jag.2016.06.013.

Mirzaee, S., Falk, A., Heresh, F., 2023. Non-linear phase linking using joined distributed and persistent scatterers. Comput. Geosci. 171, 105291. https://doi.org/10.1016/j.cageo.2022.105291.

Moser, G., Zerubia, J., Serpico, S.B., 2006. SAR amplitude probability density function estimation based on a generalized Gaussian model. IEEE Trans. Image Process. 15, 1429–1442. https://doi.org/10.1109/TIP.2006.871124.

Oduoye, M.O., Karim, K.A., Kareem, M.O., Shehu, A., Oyeleke, U.A., Zafar, H., Muhsin Umar, M., Raja, H.A.A., Adegoke, A.A., 2024. Flooding in Libya amid an economic crisis: what went wrong? IJS Glob. Health 7, e0401.

Papoutsis, I., Kontoes, C., Alatza, S., Apostolakis, A., Loupasakis, C., 2020. InSAR greece with parallelized persistent scatterer interferometry: a national ground motion service for big copernicus Sentinel-1 data. Remote Sens. 12, 3207. https://doi.org/10.3390/rs12193207.

Pepe, A., Yang, Y., Manzo, M., Lanari, R., 2015. Improved EMCF-SBAS processing chain based on advanced techniques for the noise-filtering and selection of small baseline multi-look DInSAR interferograms. IEEE Trans. Geosci. Remote Sens. 53, 4394–4417. https://doi.org/10.1109/TGRS.2015.2396875.

Reinisch, E.C., Cardiff, M., Feigl, K.L., 2017. Graph theory for analyzing pair-wise data: application to geophysical model parameters estimated from interferometric synthetic aperture radar data at Okmok volcano, Alaska. J. Geod. 91, 9–24. https://doi.org/10.1007/s00190-016-0934-5.

Ruiz-Armenteros, A.M., Delgado, J.M., Bakon, M., Sousa, J.J., Lamas-Fernandez, F., Marchamalo-Sacristan, M., Sanchez-Ballesteros, V., Papco, J., Gonzalez-Rodrigo, B., Lazecky, M., Perissin, D., 2021. ReMoDams: Monitoring Dams from Space Using

Satellite Radar Interferometry. In: 2021 IEEE International Geoscience and Remote Sensing Symposium IGARSS. Presented at the IGARSS 2021 - 2021 IEEE International Geoscience and Remote Sensing Symposium, IEEE, Brussels, Belgium, pp. 5331–5334. doi: 10.1109/IGARSS47720.2021.9553375.

Shen, P., Wang, C., An, B., 2023. AdpPL: An adaptive phase linking-based distributed scatterer interferometry with emphasis on interferometric pair selection optimization and adaptive regularization. Remote Sens. Environ. 295, 113687. https://doi.org/10.1016/j.rse.2023.113687.

Smittarello, D., d'Oreye, N., Jaspard, M., Derauw, D., Samsonov, S., 2022. Pair selection optimization for InSAR time series processing. J. Geophys. Res. Solid Earth 127, e2021JB022825. https://doi.org/10.1029/2021JB022825.

Song, C., Fan, C., Zhu, J., Wang, J., Sheng, Y., Liu, K., Chen, T., Zhan, P., Luo, S., Yuan, C., Ke, L., 2022. A comprehensive geospatial database of nearly 100 000 reservoirs in China. Earth Syst. Sci. Data 14, 4017–4034. https://doi.org/10.5194/essd-14-4017-2022.

Tavakkoliestahbanati, A., Milillo, P., Kuai, H., Giardina, G., 2024. Pre-collapse spaceborne deformation monitoring of the Kakhovka dam, Ukraine, from 2017 to 2023. Commun. Earth Environ. 5, 145. https://doi.org/10.1038/s43247-024-01284-z.

Tedd, P., Charles, C.J.A., Holton, I.R., Robertshaw, A.C., 1997. The effect of reservoir drawdown and long-term consolidation on the deformation of old embankment dams. Géotechnique 47, 33–48. https://doi.org/10.1680/geot.1997.47.1.33.

Terzaghi, K., Peck, R.B., Mesri, G., 1996. Soil mechanics in engineering practice, 3rd ed. Wiley, New York.

Tomás, R., Cano, M., García-Barba, J., Vicente, F., Herrera, G., Lopez-Sanchez, J.M., Mallorquí, J.J., 2013. Monitoring an earthfill dam using differential SAR interferometry: La Pedrera dam, Alicante. Spain. Eng. Geol. 157, 21–32. https://doi.org/10.1016/j.enggeo.2013.01.022.

Verma, D., Vijay, S., 2024. Time-Series Analysis of Dam Deformation Using Satellite-Based InSAR Technique: Case Studies from Oroville, Pong, and Tehri Dams, in: IGARSS 2024 - 2024 IEEE International Geoscience and Remote Sensing Symposium. Presented at the IGARSS 2024 - 2024 IEEE International Geoscience and Remote Sensing Symposium, IEEE, Athens, Greece, pp. 11136–11140. doi: 10.1109/IGARSS53475.2024.10642554.

Wang, J., Walter, B.A., Yao, F., Song, C., Ding, M., Maroof, A.S., Zhu, J., Fan, C., McAlister, J.M., Sikder, S., Sheng, Y., Allen, G.H., Crétaux, J.-F., Wada, Y., 2022. GeoDAR: georeferenced global dams and reservoirs dataset for bridging attributes and geolocations. Earth Syst. Sci. Data 14, 1869–1899. https://doi.org/10.5194/essd-14-1869-2022.

Wang, S., Gu, C., Liu, Y., Gu, H., Xu, B., Wu, B., 2024. Displacement observation data-based structural health monitoring of concrete dams: a state-of-art review. Structures 68, 107072. https://doi.org/10.1016/j.istruc.2024.107072.

Wang, Y., Xu, H., Zeng, G., Liu, W., Li, S., Li, C., 2023. A method for selecting SAR interferometric pairs based on coherence spectral clustering. IEEE Trans. Geosci. Remote Sens. 61, 1–15. https://doi.org/10.1109/TGRS.2023.3327260.

Wang, Y., Zhu, X.X., Bamler, R., 2012. Retrieval of phase history parameters from distributed scatterers in urban areas using very high resolution SAR data. ISPRS J. Photogramm. Remote Sens Innovative Applications of SAR Interferometry from Modern Satellite Sensors 73, 89–99. https://doi.org/10.1016/j.isprsjprs.2012.06.007.

Wu, H., Zhang, Y., Kang, Y., Lu, Z., Cheng, X., 2019. Semi-automatic selection of optimum image pairs based on the interferometric coherence for time series SAR interferometry. Remote Sens. Lett. 10, 1105–1112. https://doi.org/10.1080/2150704X.2019.1650981.

Xiao, R., Jiang, M., Li, Z., He, X., 2022. New insights into the 2020 Sardoba dam failure in Uzbekistan from Earth observation. Int. J. Appl. Earth Obs. Geoinformation 107, 102705. https://doi.org/10.1016/j.jag.2022.102705.

Xie, L., Xu, W., Ding, X., 2022a. Precursory motion and deformation mechanism of the 2018 Xe Pian-Xe Namnoy dam Collapse, Laos: insights from satellite radar interferometry. Int. J. Appl. Earth Obs. Geoinformation 109, 102797. https://doi.org/10.1016/j.jag.2022.102797.

Xie, L., Xu, W., Ding, X., Bürgmann, R., Giri, S., Liu, X., 2022b. A multi-platform, open-source, and quantitative remote sensing framework for dam-related hazard investigation: insights into the 2020 Sardoba dam collapse. Int. J. Appl. Earth Obs. Geoinformation 111, 102849. https://doi.org/10.1016/j.jag.2022.102849.

Xu, B., Yang, D., Yao, P., Burnett, W.C., Ran, X., Charette, M., Huang, X., Liu, S., Yu, Z., 2018. A new perspective for assessing water transport and associated retention effects in a large reservoir. Geophys. Res. Lett. 45, 9642–9650. https://doi.org/10.1029/2018GL079687.

Yu, C., Li, Z., Penna, N.T., Crippa, P., 2018. Generic atmospheric correction model for interferometric synthetic aperture radar observations. J. Geophys. Res. Solid Earth 123, 9202–9222. https://doi.org/10.1029/2017JB015305.

Zhang, Z., Li, J., Duan, P., Chang, J., 2023. Creep identification by the baseline optimized TS-InSAR technique considering the monthly variation in coherence. Geocarto Int. 38, 2159071. https://doi.org/10.1080/10106049.2022.2159071.

Zheng, Y., Fattahi, H., Agram, P., Simons, M., Rosen, P., 2022. On closure phase and systematic bias in multilooked SAR interferometry. IEEE Trans. Geosci. Remote Sens. 60, 1–11. https://doi.org/10.1109/TGRS.2022.3167648.

He, Z., Yu, H., Xie, S., Yu, L., Chen, L., 2022. Deformation monitoring of Xiaolangdi dam based on SBAS-InSAR technology. Sci. Surv. Map. (in Chinese) 47 (5), 66–72. https://doi.org/10.16251/j.cnki.1009-2307.2022.05.009.

Hu, G., Jiang, J., Qiu, W., Liu, Q., 2004. Outer deformation monitoring and data analysis of the dam of Xiaolangdi Multipurpose Project. Water Power (in Chinese) 30 (9), 49–51.

Zhao Q., 2010. Research & application of the multi-point statistical model on dam deformation analysis [Doctoral thesis, Wuhan University].